

# Orbits in bootstrapped Newtonian gravity

Anna D’Addio,<sup>1,2,\*</sup> Roberto Casadio,<sup>3,4,†</sup> Andrea Giusti,<sup>5,‡</sup> and Mariafelicia De Laurentis<sup>1,2,6,§</sup>

<sup>1</sup>*Dipartimento di Fisica “E. Pancini”, Università di Napoli “Federico II”,  
Compl. Univ. di Monte S. Angelo, via Cinthia Edificio 6, 80126 Napoli, Italy*

<sup>2</sup>*I.N.F.N., Sezione di Napoli, Compl. Univ. di Monte S. Angelo, via Cinthia Edificio 6, 80126 Napoli, Italy*

<sup>3</sup>*Dipartimento di Fisica e Astronomia “A. Righi”, Università di Bologna, via Irnerio 46, 40126 Bologna, Italy*

<sup>4</sup>*I.N.F.N., Sezione di Bologna, I.S. FLAG, viale B. Pichat 6/2, 40127 Bologna, Italy.*

<sup>5</sup>*Institute for Theoretical Physics, ETH Zurich, Wolfgang Pauli Strasse 27, 8093 Zurich, Switzerland.*

<sup>6</sup>*Lab. Theor. Cosmology, Tomsk State University, 634050 Tomsk, Russia.*

(Dated: October 19, 2021)

Bootstrapped Newtonian gravity is a non-linear version of Newton’s law which can be lifted to a fully geometric theory of gravity starting from a modified potential. Here, we study geodesics in the bootstrapped Newtonian effective metric in *vacuum* and obtain bounds on a free parameter from Solar System data and *S*-star orbits near our Galaxy centre. These bounds make *vacuum* bootstrapped Newtonian gravity experimentally indistinguishable from General Relativity.

## I. INTRODUCTION

General Relativity is presently the most successful theory for describing the gravitational interaction at the classical level. Its own failure is marked by the prediction of the formation of geodesic singularities whenever a trapped surface arises from the gravitational collapse of a compact object [1].<sup>1</sup> Such considerations open up the possibility that significant departures from General Relativity might occur where our experimental data do not yet place strong enough constraints, like for example in regions of strong gravity near a very massive source. However, Einstein’s field equations are not linear and this makes it difficult to modify the laws of gravity in the strong field regime without affecting also the weak-field behaviour, since these regimes are likely to be related non-trivially in any nonlinear theories.

The bootstrapped Newtonian gravity [3, 4] is an attempt at investigating these issues in a somewhat simplified context. This approach, based on Deser’s conjecture [6], consists of retrieving the full Einstein’s theory including gravitational self-coupling terms in the Fierz-Pauli action on flat spacetime.<sup>2</sup> These additional terms must be consistent with diffeomorphism invariance, in order to preserve the covariance of any (modified) metric theory. We can obtain different modified gravitational theories depending on the choice of boundary conditions in the reconstruction procedure [8]. A key observation is that a practically effective dynamics can be derived only starting with a “small” contribution of matter sources. For large astrophysical sources, this implies that the matter source must also be included in a non-perturbative way. In the present approach this task is addressed starting from

the Fierz-Pauli action corresponding to the potential generated by an arbitrarily large static source, and putting in extra-terms representing gravitational self-coupling. Furthermore, the coupling constants for the additional terms are not fixed to their Einstein-Hilbert values in order to accommodate for diverse underlying dynamics. This approach then results in a nonlinear equation including pressure effects and the gravitational self-interaction terms to next-to-leading order in the Newton constant, whose solution is the gravitational potential operating on test particles at rest. Such an equation was used to investigate compact objects [9–11] and coherent quantum states [12, 13].<sup>3</sup>

The motion of (test) particles and photons in the surroundings of a compact object represents the most immediate tool to gather information on the gravitational potential in which they revolve. In Ref. [16], a full (effective) metric tensor was obtained from the bootstrapped Newtonian potential, which allows one to study these trajectories in general, and to compare them with results from General Relativity. The requirement that the resulting theory of gravity is covariant is satisfied by the use of an effective metric tensor, since the bootstrapped Newtonian dynamics is implicitly assumed to be invariant under coordinate transformations. Nonetheless, the particular metric found in Ref. [16] differs from the Schwarzschild geometry, hence it is not a solution of the Einstein equations in the vacuum. An effective fluid is therefore present, as was already noted in the cosmological context [17].

The bootstrapped effective metric is given as a function of parameterised post-Newtonian (PPN) parameters [5] in the weak-field expansion. These parameters can be consistently chosen so as to minimise deviations from the Schwarzschild metric only up to a point. In fact, some of the PPN parameters are uniquely related and, at the PPN order determined in Ref. [16], they can be expressed in terms of one free parameter. In this work, we report on a phenomenological in-

\*Electronic address: [anna.daddio@unina.it](mailto:anna.daddio@unina.it)

†Electronic address: [casadio@bo.infn.it](mailto:casadio@bo.infn.it)

‡Electronic address: [agiusti@phys.ethz.ch](mailto:agiusti@phys.ethz.ch)

§Electronic address: [mariafelicia.delarentis@unina.it](mailto:mariafelicia.delarentis@unina.it)

<sup>1</sup> We also recall that point-like sources are mathematically incompatible with the Einstein field equations [2].

<sup>2</sup> This idea is indeed older, see e.g. Ref. [7].

<sup>3</sup> These quantum states show some of the properties [14] found in the corpuscular model of black holes [15]. However, we shall not discuss quantum aspects in this work.

vestigation aiming at placing bounds on this remaining free parameter from the measured precessions in the Solar System [18, 19, 21, 22] and from the study of  $S$ -star orbits around the black hole in the centre of the Galaxy [23–28].

The paper is organised as follows: in Section II, we briefly review the equation for the bootstrapped Newtonian potential and its solution in the vacuum. We then just recall the full effective metric reconstructed from this potential, which is then used to analyse Solar System data and  $S$ -star motions in Section III; we conclude with comments and an outlook in Section IV.

## II. BOOTSTRAPPED NEWTONIAN VACUUM

We shall only review briefly the derivation of the bootstrapped Newtonian equation, since all the details can be found in Refs. [3, 9, 11, 13]. We shall use units with the speed of light  $c = 1$  in this section. We start from the Lagrangian for the Newtonian potential  $V = V(r)$  generated by a static and spherically symmetric source of density  $\rho = \rho(r)$ , to wit

$$L_N[V] = -4\pi \int_0^\infty r^2 dr \left[ \frac{(V')^2}{8\pi G_N} + V\rho \right], \quad (\text{II.1})$$

where primes denote derivatives with respect to  $r$ . The corresponding Euler-Lagrange field equation is given by Poisson's

$$\frac{1}{r^2} \frac{d}{dr} \left( r^2 \frac{dV}{dr} \right) = 4\pi G_N \rho, \quad (\text{II.2})$$

where we recall that the radial coordinate  $r$  is the one obtained from harmonic coordinates [5, 16]. We next couple  $V$  to a gravitational current proportional to its own energy density,

$$J_V \simeq 4 \frac{dU_N}{dV} = -\frac{[V'(r)]^2}{2\pi G_N}, \quad (\text{II.3})$$

where  $\mathcal{V}$  is the spatial volume and  $U_N$  the Newtonian potential energy. We also add the ‘‘one loop term’’  $J_\rho \simeq -2V^2$ , which couples to  $\rho$ , and the pressure term  $p$  [9]. The total Lagrangian then reads

$$L[V] = -4\pi \int_0^\infty r^2 dr \left[ \frac{(V')^2}{8\pi G_N} (1 - 4q_V V) + (\rho + 3q_p p) V (1 - 2q_\rho V) \right], \quad (\text{II.4})$$

where the coupling constants  $q_V$ ,  $q_p$  and  $q_\rho$  can be used to track the effects of the different contributions. For instance, the case  $q_V = q_p = q_\rho = 1$  reproduces the Einstein-Hilbert action at next-to-leading order in perturbations around Minkowski [9, 11, 13]. Finally, the bootstrapped Newtonian field equation reads

$$\frac{1}{r^2} \frac{d}{dr} \left( r^2 \frac{dV}{dr} \right) = 4\pi G_N \frac{1 - 4q_\rho V}{1 - 4q_V V} (\rho + 3q_p p) + \frac{2q_V (V')^2}{1 - 4q_V V}, \quad (\text{II.5})$$

which must be solved along with the conservation equation  $p' = -V'(\rho + p)$ .

### A. Vacuum potential

In vacuum, we have  $\rho = p = 0$  and Eq. (II.5) simplifies to

$$\frac{1}{r^2} \frac{d}{dr} \left( r^2 \frac{dV}{dr} \right) = \frac{2q (V')^2}{1 - 4qV}, \quad (\text{II.6})$$

where we renamed  $q \equiv q_V$  for simplicity. The exact solution was found in Ref. [3] and reads

$$V(r) = \frac{1}{4q} \left[ 1 - \left( 1 + \frac{6q G_N M}{r} \right)^{2/3} \right], \quad (\text{II.7})$$

The asymptotic expansion away from the source yields

$$V_2 \simeq -\frac{G_N M}{r} + q \frac{G_N^2 M^2}{r^2} - q^2 \frac{8 G_N^3 M^3}{3 r^3}, \quad (\text{II.8})$$

so that the Newtonian behaviour is always recovered (for  $q = 0$ ) and the post-Newtonian terms are seen to depend on the coupling  $q$  (see Fig. 1).

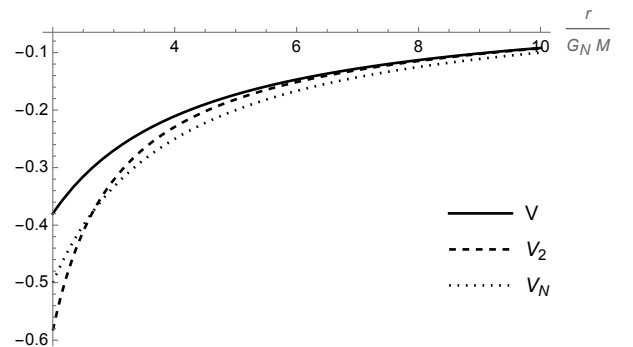


Figure 1: Bootstrapped Newtonian potential  $V$  in Eq. (II.7) compared to its expansion  $V_2$  from Eq. (II.8) and to the Newtonian potential  $V_N$  (for  $q = 1$ ).

### B. Vacuum effective metric

A complete space-time metric was reconstructed from the vacuum potential (II.7) in Ref. [16]. The procedure is rather cumbersome and we shall here only recall a few main steps leading to the necessary expressions in the weak-field regime. We explicitly show the speed of light  $c$  from here on. One starts from the PPN form [5]

$$ds^2 \simeq \left[ 1 - \alpha \frac{2R_g}{\bar{r}} + (\beta - \alpha\gamma) \frac{2R_g^2}{\bar{r}^2} + (\zeta - 1) \frac{8R_g^3}{\bar{r}^3} \right] c^2 dt^2 + \left[ 1 + \gamma \frac{2R_g}{\bar{r}} + \xi \frac{4R_g^2}{\bar{r}^2} + \sigma \frac{8R_g^3}{\bar{r}^3} \right] d\bar{r}^2 + \bar{r}^2 d\Omega^2, \quad (\text{II.9})$$

where  $R_g = G_N M/c^2$  and  $\bar{r}$  is the areal radius, which differs from the radial coordinate  $r$  in which the potential (II.7) is expressed. The latter is obtained from harmonic coordinates and the two radial coordinates are related by [16]

$$r \simeq \bar{r} + (1 - 3\gamma) \frac{R_g}{2} + (1 - 3\gamma + 2\gamma^2 - 2\Xi) \frac{R_g^2}{\bar{r}}, \quad (\text{II.10})$$

in which  $\Xi$  is a free parameter. Furthermore, we have

$$q = \beta + \frac{\gamma - 1}{2}. \quad (\text{II.11})$$

We can next set  $\alpha = 1$  by simply absorbing this coefficient in the definition of the mass  $M$  [29], and  $\beta = \gamma = 1$  in order to satisfy the experimental constraints  $|\gamma - 1| \simeq |\beta - 1| \ll 1$ . From Eq. (II.11), this is tantamount to set  $q = 1$ , as expected. The higher order PPN parameters are then fully determined by  $\Xi$  according to

$$\xi = 1 + \Xi \quad (\text{II.12})$$

$$\zeta = 1 - \frac{5 + 6\Xi}{12} = \frac{13 - 6\Xi}{12} \quad (\text{II.13})$$

$$\sigma = \frac{9 + 14\Xi}{4}. \quad (\text{II.14})$$

As already noted in Ref. [16], the General Relativistic PPN combination  $\xi = \zeta = 1$  cannot be obtained for any value of  $\Xi$  and the bootstrapped metric for which we have the minimum deviation from the Schwarzschild form is thus given by

$$ds^2 \simeq - \left[ 1 - \frac{2R_g}{r} - (5 + 6\Xi) \frac{2R_g^3}{3c^6 r^3} \right] c^2 dt^2 + \left[ 1 + \frac{2R_g}{r} + (1 + \Xi) \frac{4R_g^2}{r^2} + (9 + 14\Xi) \frac{2R_g^3}{r^3} \right] dr^2 + r^2 d\Omega^2, \quad (\text{II.15})$$

in which we drop the bar from the areal coordinate for simplicity from now on. We can see that there are contributions in the metric coefficients which cannot be reduced to the Schwarzschild expressions. This deviation from the Schwarzschild solution is encoded by the free parameter  $\Xi$ , whose value is a priori unknown and must be constrained by observations. In particular, we will test these corrections by analysing the planets in the Solar System and S-stars motion around Sgr A\*.

The geodesic equations

$$\ddot{x}^\mu + \Gamma_{\alpha\beta}^\mu \dot{x}^\alpha \dot{x}^\beta = 0, \quad (\text{II.16})$$

where a dot indicates the derivative with respect to the proper time, can be equivalently computed using the Euler-Lagrange equations

$$\frac{d}{ds} \left( \frac{\partial L}{\partial \dot{x}^\mu} \right) - \frac{\partial L}{\partial x^\mu} = 0, \quad (\text{II.17})$$

with  $L = g_{\alpha\beta} \dot{x}^\alpha \dot{x}^\beta = -1$  for a massive object. From the metric in Eq. (II.15), one then finds

$$\ddot{t} = \frac{6\dot{r}\dot{t}[(5 + 6\Xi)R_g^3 + R_g r^2]}{2(5 + 6\Xi)R_g^3 r + 6R_g r^3 - 3r^4} \quad (\text{II.18})$$

and

$$\ddot{\theta} = \dot{\phi}^2 \sin\theta \cos\theta - \frac{2\dot{r}\dot{\theta}}{r}, \quad (\text{II.19})$$

which are the usual conservation equations for the angular momentum and the energy conjugated to  $t$ , respectively. Moreover,

$$\ddot{\phi} = -\frac{2\dot{\phi}}{r} (\dot{r} + r\dot{\theta} \cot\theta) \quad (\text{II.20})$$

and spherical symmetry as usual implies that the orbital motion occurs on a plane ( $\dot{\theta} = 0$ ) which we can arbitrarily set at  $\theta = \pi/2$ . Finally, radial motion is governed by

$$\ddot{r} = \frac{R_g \{ 4(1 + \Xi) R_g r \dot{r}^2 + R_g^2 [ 3(9 + 14\Xi) \dot{r}^2 - c^2 (5 + 6\Xi) \dot{t}^2 ] + r^2 (\dot{r}^2 - c^2 \dot{t}^2) \} + r^5 (\dot{\theta}^2 + \dot{\phi}^2 \sin^2\theta)}{r [ 2(9 + 14\Xi) R_g^3 + 4(1 + \Xi) R_g^2 r + 2R_g r^2 + r^3 ]}. \quad (\text{II.21})$$

The above parametric system of non-linear differential equations can be integrated numerically in order to study the orbits.

### 1. Precession

It is easy to express the perihelion precession in terms of the PPN parameters [5]. At leading order, one has

$$\Delta\phi^{(1)} = 2\pi(2 - \beta + 2\gamma) \frac{R_g}{\ell}, \quad (\text{II.22})$$

where  $\ell = a(1 - \epsilon^2)$  is the *semilatus rectum*,  $a$  is the semi-major axis and  $\epsilon$  the eccentricity. For  $\beta = \gamma = 1$ , Eq. (II.22) reproduces the General Relativistic result

$$\Delta\phi_S^{(1)} = 6\pi \frac{R_g}{\ell}. \quad (\text{II.23})$$

The second order correction depends on  $\xi$  and  $\zeta$  and, for  $\beta = \gamma = 1$ , it reads [16]

$$\begin{aligned} \Delta\phi^{(2)} &= \pi \left[ (41 + 10\xi - 24\zeta) + (16\xi - 13) \frac{\epsilon^2}{2} \right] \frac{R_g^2}{\ell^2} \\ &\simeq \pi \left[ (37 + 22\Xi) + (3 + 16\Xi) \frac{\epsilon^2}{2} \right] \frac{R_g^2}{\ell^2} \\ &\simeq \Delta\phi_S^{(2)} + 2\pi [11\xi - 7 + 4(\xi - 1)\epsilon^2] \frac{R_g^2}{\ell^2}, \end{aligned} \quad (\text{II.24})$$

where the General Relativistic result  $\Delta\phi_S^{(2)}$  corresponds to  $\xi = \zeta = 1$ . From Eqs. (II.12) and (II.13), it follows that we cannot have  $\xi = \zeta = 1$  for any value of  $\Xi$ , and a deviation from General Relativity remains.

### III. ASTRONOMICAL TESTS

In order to constrain the free parameter of the bootstrapped Newtonian potential,  $\Xi$ , we confronted the theoretical results exposed in Sec. II B with astronomical data.

To infer a range of validity for  $\Xi$ , we compared the analytical expression of the precession with the observed values of the perihelion advance of Solar System's planets (Sec. III A).

Then, we turned our attention to the Galactic Center and we studied the motion of  $S$ -Stars orbiting around Sgr A\*. To constrain  $\Xi$ , we let it vary in a given range and fit the corresponding simulated orbits to astrometric observations. In particular, we adopted a fully relativistic approach which consists of integrating numerically Eqs. (II.18)-(II.21) in order to get the mock orbits, instead of solving Newton's law with the standard potential replaced by the modified one.

#### A. Perihelion precession in the Solar System

In order to constrain  $\Xi$  we can start from the Solar System planets whose orbital precession has been measured, namely Mercury, Venus, Earth, Mars, Jupiter and Saturn [36]. The confidence region for  $\Xi$  can be identified as the set of values such that the precession

$$\Delta\phi = \Delta\phi^{(1)} + \Delta\phi^{(2)} \quad (\text{III.1})$$

is compatible with the observations. The planetary parameters,<sup>4</sup> the corresponding observed values of the precession [36] and the General Relativistic value obtained by

Eq. (II.23) are reported in Table I from first to seventh column. The allowed region of  $\Xi$  for each planet is defined as the range of values compatible with data, having as extremes the values of  $\Xi$  solving the equation

$$\Delta\phi = \Delta\phi_{obs}. \quad (\text{III.2})$$

The inferred lower and upper limits on  $\Xi$  are reported in the last column of Table I and the included area is depicted in Figure 2 for each planet (grey shades). It is worth noticing the discrepancy between the General Relativistic value (the red line) and the observed precession (blue dashed lines) for Mars and Jupiter; it could be attributed to the incomplete subtraction of non-relativistic effects from the observed value, complicated by the presence of the asteroid belt between Mars and Jupiter, and the presence of an anomalous residual precession [36, 37].

The tightest interval on the parameter  $\Xi$  is obtained with Venus, for which it can vary between  $-1149.67$  and  $1167.47$ . We can use the values defining such an interval to predict the precession for Uranus, Neptune and Pluto, for which no observation is available. The results, summarised in Table II, show that the bootstrapped theory predictions are in perfect agreement with General Relativity.

Now it is useful to move to a different scale and analyse  $S2$  (see Table III), the only one among the  $S$ -stars whose precession was observed [33]. The results, summed up in Table IV, confirm the compatibility of our predictions with General Relativity. We can next calculate the precession for Mars, Jupiter and  $S2$  with the values of  $\Xi$  as obtained by Mercury, Venus, Earth and Saturn to check agreement with the corresponding Schwarzschild value and with the observations (see Table IV). The mean value of the parameter  $\Xi$  such that

$$\Delta\phi = \Delta\phi_S \quad (\text{III.3})$$

is given by

$$\Xi = -1.64236 \pm 0.10305. \quad (\text{III.4})$$

#### B. $S$ -star dynamics

We can confirm the bounds on  $\Xi$  deduced from orbital precessions by comparing them with results deduced from the analysis of stellar orbits at the Galactic Center. This further analysis consists in comparing simulated orbits in bootstrapped Newtonian gravity, obtained by integrating numerically Eqs. (II.21)-(II.18), with observed orbits of three  $S$ -stars constructed by astrometric observations (see Sec. III B 1). In particular, we focused on stars  $S2$ ,  $S38$  and  $S55$  for two main reasons: among the brightest stars they are those with the shortest period. These properties are desired because highly bright stars are less prone to be confused with other sources, and a short period allow us to observe a larger part of the orbit in a given observation session. For simplicity, we neglected perturbations from other members of the cluster and any extended matter structures.

<sup>4</sup>The reported values are taken from NASA fact sheet at <https://nssdc.gsfc.nasa.gov/planetary/factsheet/>

Planet	$a(10^6 km)$	$P(years)$	$i(^{\circ})$	$e$	$\Delta\phi_{obs}(''/cy)$	$\Delta\phi_S(''/cy)$	$[\Xi_{min}; \Xi_{max}]$
<b>Mercury</b>	57.909	0.24	7.005	0.2056	$43.1000 \pm 0.5000$	42.9822	$[-89708.7; 144995]$
<b>Venus</b>	108.209	0.61	3.395	0.0067	$8.6247 \pm 0.0005$	8.6247	$[-1149.67; 1167.47]$
<b>Earth</b>	149.596	1.00	0.000	0.0167	$3.8387 \pm 0.0004$	3.83881	$[-3660.86; 2094.96]$
<b>Mars</b>	227.923	1.88	1.851	0.0935	$1.3565 \pm 0.0004$	1.35106	$[155248.; 179879.]$
<b>Jupiter</b>	778.570	11.86	1.305	0.0489	$0.6000 \pm 0.3000$	0.0623142	$[5.46709 \times 10^8; 1.92679 \times 10^9]$
<b>Saturn</b>	1433.529	29.45	2.485	0.0565	$0.0105 \pm 0.0050$	0.0136394	$[-1.57315 \times 10^8; 3.59618 \times 10^7]$

Table I: Values of semi-major axis ( $a$ ), orbital period ( $P$ ), tilt angle ( $i$ ), eccentricity ( $e$ ), observed orbital precession ( $\Delta\phi_{obs}$ ), orbital precession as predicted by General Relativity ( $\Delta\phi_S$ ) and constraints on  $\Xi$  for Solar System's planets.

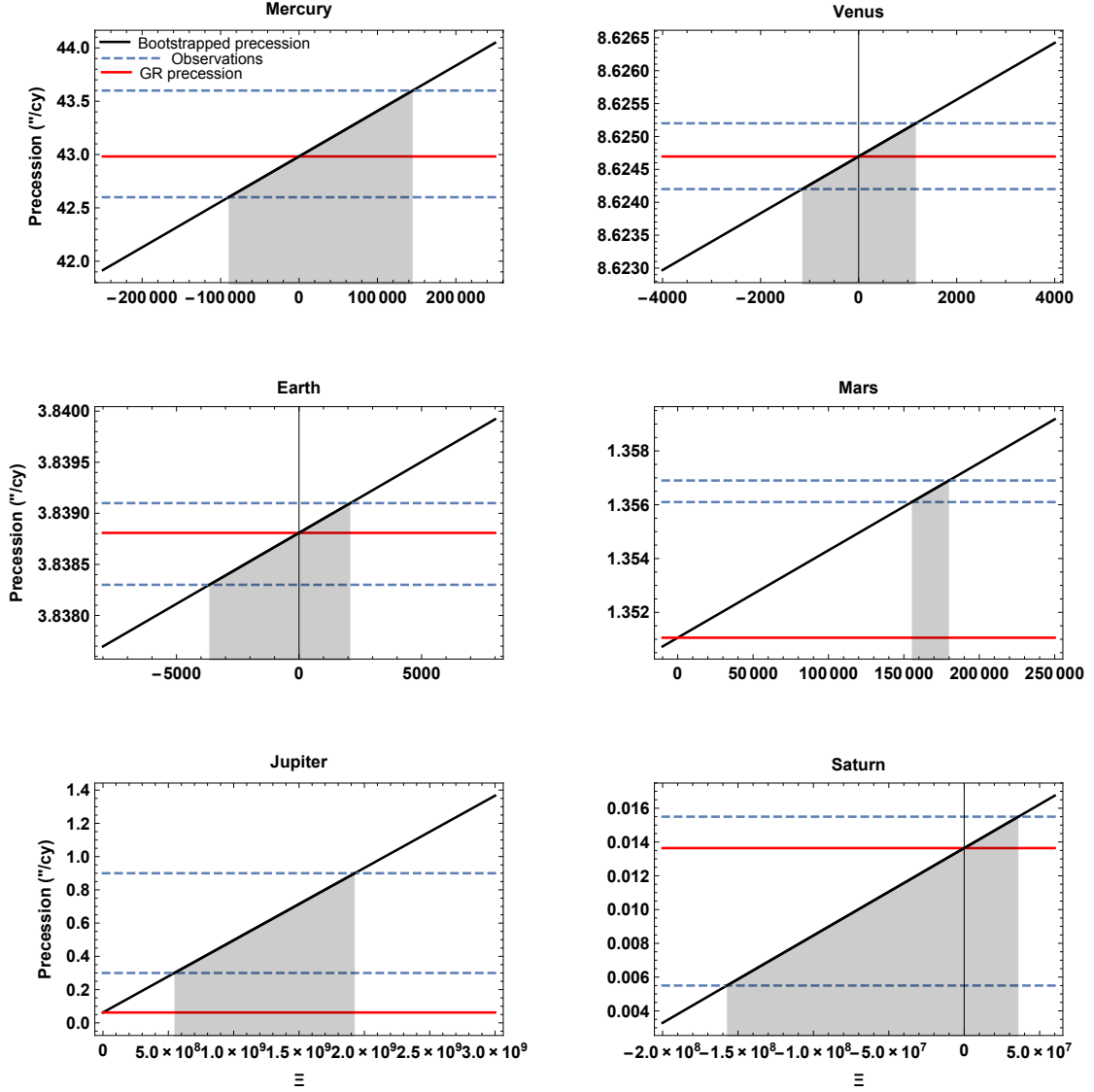


Figure 2: Bootstrapped orbital precession as a function of the parameter  $\Xi$ . Black lines give the theoretical prediction from Eq. (III.1), blue dashed lines represent the measurements adapted from [36] and red lines depict the General Relativistic values as in Eq. (II.23). Confidence regions for  $\Xi$  are shaded in grey.

Planet	$a(10^6 km)$	$P(years)$	$i(^{\circ})$	$e$	$\Delta\phi_S(^{\circ}/cy)$	$[\Delta\phi_{min}; \Delta\phi_{max}]$
<b>Uranus</b>	2872.463	84.01	0.772	0.0457	0.00238404	[0.00238404; 0.00238405]
<b>Neptune</b>	4495.060	164.786	1.769	0.0113	0.000775374	[0.000775373; 0.000775375]
<b>Pluto</b>	5869.656	247.936	17.16	0.2444	0.000419669	[0.000419669; 0.00041967]

Table II: Orbital parameters from Nasa Fact Sheet, the General Relativistic prediction for the precession in the sixth column and the values predicted by the bounds on the parameter  $\Xi$  of the Bootstrapped theory deduced for Venus (see Table V).

Star	$a(AU)$	$P(years)$	$i(^{\circ})$	$e$	$\Delta\phi_{obs}(^{\circ}/cy)$	$\Delta\phi_S(^{\circ}/cy)$	$[\Xi_{min}; \Xi_{max}]$
<b>S2</b>	1031.32	16.0455	134.567	0.884649	$730.382 \times (1.10 \pm 0.19)$	730.382	[-103.066; 326.398]

Table III: For the star  $S2$ , orbital parameters [33], observed orbital precession ( $\Delta\phi_{obs}$ ), orbital precession as predicted by General Relativity ( $\Delta\phi_S$ ) and constraints on  $\Xi$ .

### 1. Astrometric data

Astrometric data are taken from Ref. [30]<sup>5</sup> and cover 25 years of observations performed in the near-infrared (NIR), where the interstellar extinction amounts to about 3 magnitudes. Different instruments have been used, which we briefly describe below.

1. SHARP - First high-resolution data of the Galactic Center were obtained in 1992 with the SHARP camera at the ESO's 3.5 m NTT in Chile, operating in Speckle mode with exposure times of 0.3 s, 0.5 s and 1.0 s. The data, described in detail in Ref. [31], led to the detection of high proper motion near the central massive object.
2. NACO - The first Adaptive Optics (AO) imaging data were produced by Naos-Conica (NACO) system, mounted at the telescope Yepun (8.0 m) of the VLT and starting to operate in 2002. It followed a great improvement due to larger telescope aperture, and the higher Strehl ratio (about 40%).
3. GEMINI - The data-set includes observations obtained by the 8 m telescope Gemini North in Mauna Kea, Hawaii. These images, obtained using AO system in combination with the NIR camera Quirc, were processed by the Gemini team.

The astrometric calibration of these data, treated in Ref. [32], consists in the following steps: obtaining high-quality maps of the  $S$ -stars, extracting pixel positions and transforming them to a common astrometric coordinate system. In particular, the astrometric reference frame is implemented relating the  $S$ -stars positions to a set of selected reference stars, which are in turn related to a set of SiO maser stars whose positions relative to Sgr A\* is known.

<sup>5</sup> Data are publicly available on the electronic version of Ref. [30] at the link <https://iopscience.iop.org/article/10.3847/1538-4357/aa5c41/meta>.

### 2. Fitting procedure

The first step of the fitting procedure is the numerical integration of the system of parametric non-linear differential equations (II.21)-(II.18) to produce stellar simulated orbits in bootstrapped Newtonian gravity.

Preliminarily, we fix the Keplerian elements and the parameters of the central mass to the values reported in Tables V and VI. In particular, for the study of  $S2$  we used the values obtained by the Gravity Collaboration [33], and for  $S38$  and  $S55$  those obtained in Ref. [30]. In order to have a well-defined Cauchy problem, we must provide initial conditions for the four-dimensional coordinates and their derivatives with respect to the proper time:  $\{r(0), \dot{r}(0), \theta(0), \dot{\theta}(0), \phi(0), \dot{\phi}(0), t(0), \dot{t}(0)\}$ . We assume that the star initially lies on the equatorial plane of the reference system, for which  $\theta(0) = \pi/2$ , and that its initial velocity is parallel to the equatorial plane, that is  $\dot{\theta}(0) = 0$ . It then follows that  $\dot{\theta}(0) = 0$  identically. In particular, we set the initial conditions for  $r$  and  $\phi$  at the time of passage of the apocenter, when the Cartesian coordinates of the star expressed in the orbital plane are given by

$$(x_{orb}, y_{orb}) = (-a(1 + \epsilon), 0) \quad (\text{III.5})$$

and the Cartesian components of its velocity read

$$(v_{x,orb}, v_{y,orb}) = \left(0, \frac{2\pi a^2}{T r} \sqrt{1 - \epsilon^2}\right). \quad (\text{III.6})$$

The initial condition for  $\dot{t}$  can be retrieved from the normalization of four-velocities requiring that the geodesic is time-like.

Starting from the initial conditions of each star, we proceed with an explicit Runge-Kutta numerical integration of the relativistic equations of motion. The results are the stars mock orbit in the orbital plane, described by a four-dimensional array  $\{t(\tau), r(\tau), \theta(\tau), \phi(\tau)\}$ . To compare the theoretical orbits with those observed from the Earth, we must project any point  $(x_{orb}, y_{orb})$  on the orbital plane into the point  $(x, y)$  on the observer's sky plane. Such a transformation is realized by applying the Thiele-Innes formulas [34, 35]:

$$x = l_1 x_{orb} + l_2 y_{orb} \quad (\text{III.7})$$

$$y = m_1 x_{orb} + m_2 y_{orb}. \quad (\text{III.8})$$



Object	$\Delta\phi_{GR}(\prime/cy)$	$\Delta\phi(\Xi_{Mercury})$	$\Delta\phi(\Xi_{Venus})$	$\Delta\phi(\Xi_{Earth})$	$\Delta\phi(\Xi_{Saturn})$
<b>Mars</b>	1.35106	[1.34814; 1.35577]	[1.35102; 1.3511]	[1.35094; 1.35113]	[-3.75855; 2.5191]
<b>Jupiter</b>	0.0623142	[0.0622752; 0.0623773]	[0.0623137; 0.0623147]	[0.0623126; 0.0623151]	[-0.00607962; 0.0779489]
<b>S2</b>	730.382	[-57243.9; 94435.7]	[-11.7295; 1485.75]	[-1634.61; 2085.15]	[-1.01666 * 10 <sup>8</sup> ; 2.32414 * 10 <sup>7</sup> ]

Table IV: Precession for Mars, Jupiter and *S2* as predicted by confidence regions for  $\Xi$  inferred from Mercury, Venus, Earth and Saturn.

Parameter	S2	S38	S55
$a$ (mas)	125.058 $\pm$ 0.041	141.6 $\pm$ 0.2	107.8 $\pm$ 1.0
$\Omega$ ( $^\circ$ )	228.171 $\pm$ 0.031	101.06 $\pm$ 0.24	325.5 $\pm$ 4.0
$\epsilon$	0.884649 $\pm$ 0.000066	0.8201 $\pm$ 0.0007	0.7209 $\pm$ 0.0077
$i$ ( $^\circ$ )	134.567 $\pm$ 0.033	171.1 $\pm$ 2.1	150.1 $\pm$ 2.2
$\omega$ ( $^\circ$ )	66.263 $\pm$ 0.031	17.99 $\pm$ 0.25	331.5 $\pm$ 3.9
$t_p$ (yr)	2018.37900 $\pm$ 0.00016	2003.19 $\pm$ 0.01	2009.34 $\pm$ 0.04
$T$ (yr)	16.0455 $\pm$ 0.0013	19.2 $\pm$ 0.02	12.80 $\pm$ 0.11
$m_K$	13.95	17.	17.5
Ref.	[33]	[30]	[30]

Table V: Orbital parameters of *S2*, *S38*, and *S55*: semi-major axis  $a$ , eccentricity  $\epsilon$ , inclination  $i$ , angle of the line of node  $\Omega$ , angle from ascending node to pericenter  $\omega$ , orbital period  $T$  and the time of the pericenter passage  $t_p$ .

The Thiele-Innes elements  $l_1$ ,  $l_2$ ,  $m_1$  and  $m_2$  depend on the Keplerian elements by according to

$$l_1 = \cos \Omega \cos \omega - \sin \Omega \sin \omega \cos i \quad (\text{III.9})$$

$$l_2 = -\cos \Omega \sin \omega - \sin \Omega \cos \omega \cos i \quad (\text{III.10})$$

$$m_1 = \sin \Omega \cos \omega + \cos \Omega \sin \omega \cos i \quad (\text{III.11})$$

$$m_2 = -\sin \Omega \sin \omega + \cos \Omega \cos \omega \cos i. \quad (\text{III.12})$$

The second step consists in the fitting procedure itself, and has the aim to constrain the parameter  $\Xi$ . Guided by the results obtained from the precession in Sec. II B 1, we let it vary freely in an appropriate range including the value (III.4). For each value of  $\Xi$  we repeated the aforementioned procedure to get the true positions  $(x_i, y_i)$  and velocities  $(\dot{x}_i, \dot{y}_i)$  of the stars at all the observed epochs. After transforming the true positions into the apparent positions  $(x_i^{th}, y_i^{th})$ , we computed the reduced- $\chi^2$  distribution to quantify the discrepancy between theory and observations as

$$\chi_{\text{red}}^2 = \frac{1}{2N-1} \sum_i^N \left[ \left( \frac{x_i^{\text{obs}} - x_i^{\text{th}}}{\sigma_{x_i^{\text{obs}}}} \right)^2 + \left( \frac{y_i^{\text{obs}} - y_i^{\text{th}}}{\sigma_{y_i^{\text{obs}}}} \right)^2 \right], \quad (\text{III.13})$$

where  $(x_i^{\text{obs}}, y_i^{\text{obs}})$  and  $(x_i^{\text{th}}, y_i^{\text{th}})$  are respectively the observed and the predicted positions,  $N$  is the number of observations and  $(\sigma_{x_i^{\text{obs}}}, \sigma_{y_i^{\text{obs}}})$  are the observative uncertainties. Finally, we calculated the likelihood probability distribution,  $2 \log \mathcal{L} = -\chi_{\text{red}}^2(\Xi)$ . The best-fit value for  $\Xi$  was derived as the point that maximizes the likelihood distribution.

### 3. Results

Our results are summarised in Table VII, and represented in Figures 3, 4 and 5.

In Figure 3 we show the comparison between best fit and observed orbits of the selected stars: the top left panel, the

top right panel and the bottom panel illustrate the results respectively for *S2*, *S55* and *S38*. Astrometric data are reported with their own error bars to note the effectiveness of our fitting procedure.

Figure 4 depicts the comparisons between the observed and simulated coordinates with the corresponding residuals. The left column contains the right ascension (RA), while the right column reports the declination (Dec). It is worth noticing that in all stars and for both coordinates, residuals are larger at the beginning observing epochs, and decrease as astrometric accuracy improves.

Finally, we show in Figure 5 the orbits of the studied *S*-stars corresponding to the best multi-star fit for  $\Xi = 7400_{-32244.3}^{+30555.6}$  (last row of Table VII). As expected, the parameter  $\Xi$  is compatible with the the mean value (III.4) such that the bootstrapped Newtonian precession recovers General Relativity

## IV. CONCLUSIONS

In this paper we tested astronomically the Bootstrapped Newtonian gravity. The starting point is the complete space-time metric (II.15) derived in Ref. [16]. The leading order deviation from the Schwarzschild solution cannot be eliminated and is encoded in the free parameter  $\Xi$ , which is not a priori known and must be constrained by observations.

First, we showed that bounds on  $\Xi$  can be deduced from the comparison between the measurements of the orbital precession of Solar System bodies and the theoretical predictions arising from bootstrapped Newtonian metric computed in Ref. [16]. The inferred confidence region for  $\Xi$  for each planet is reported in Table I and graphically depicted in Figure 2. Based on the tightest interval obtained with Venus, we found that  $\Xi$  lies in the range  $[-1149.67; +1167.47]$ . With these values of the parameter  $\Xi$  we predicted the orbital precession for Uranus, Neptune and Pluto, and we found a theoretical precession in great agreement with the General Relativity

Star	$M(M_{\odot})$	$R(kpc)$	Ref.
S2	$(4.261 \pm 0.012) \times 10^6$	$8.2467 \pm 0.0093$	GRAVITY [33]
S38	$(4.35 \pm 0.13) \times 10^6$	$8.33 \pm 0.12$	Gillessen [30]
S55	$(4.35 \pm 0.13) \times 10^6$	$8.33 \pm 0.12$	Gillessen [30]

Table VI: Parameters of the central BH: the mass  $M$  and the distance  $R$ .

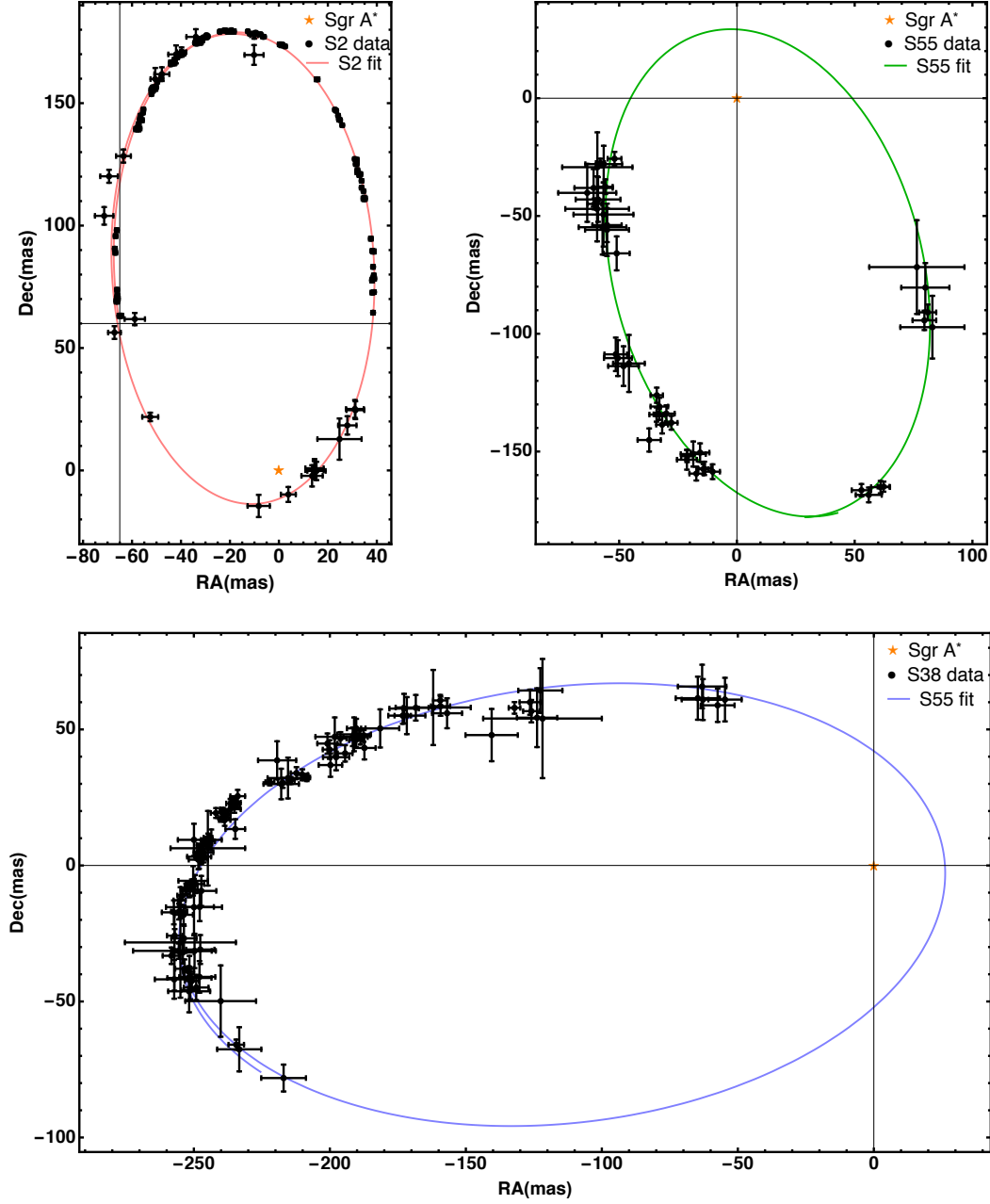


Figure 3: Comparisons between the NTT/VLT astrometric observations with their errors (black circles) and the theoretical best-fit orbits using parameters reported in the first three rows of Table VII. The results for  $S2$ ,  $S38$  and  $S55$  are illustrated respectively in the top left, top right, and bottom panels.

tivistic value. Such a compatibility was confirmed by turning our attention to the Galactic Center and repeating the same analysis for the star  $S2$  [33]. The mean value of the parameter

$\Xi$  such that the Bootstrapped Newtonian precession equals the



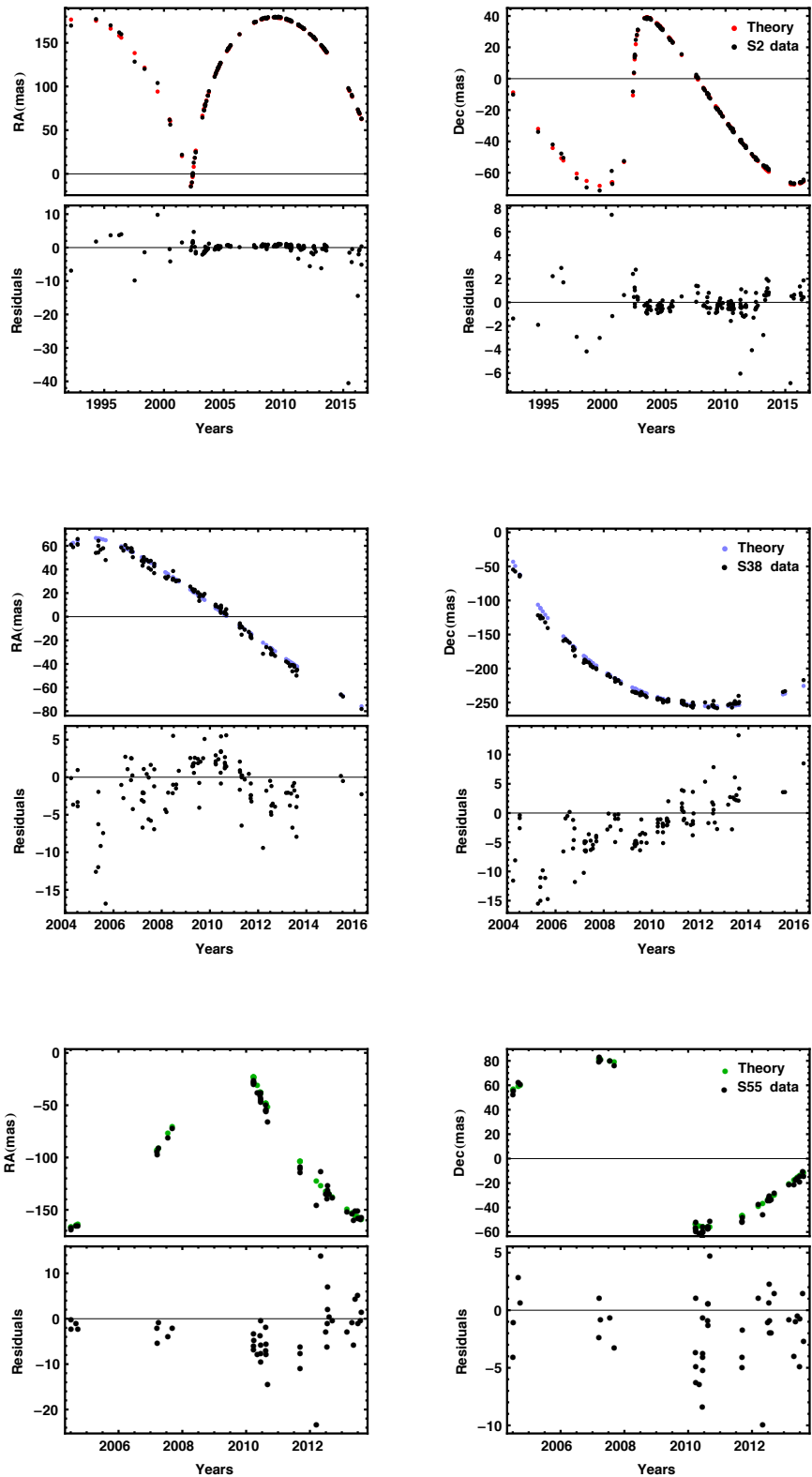
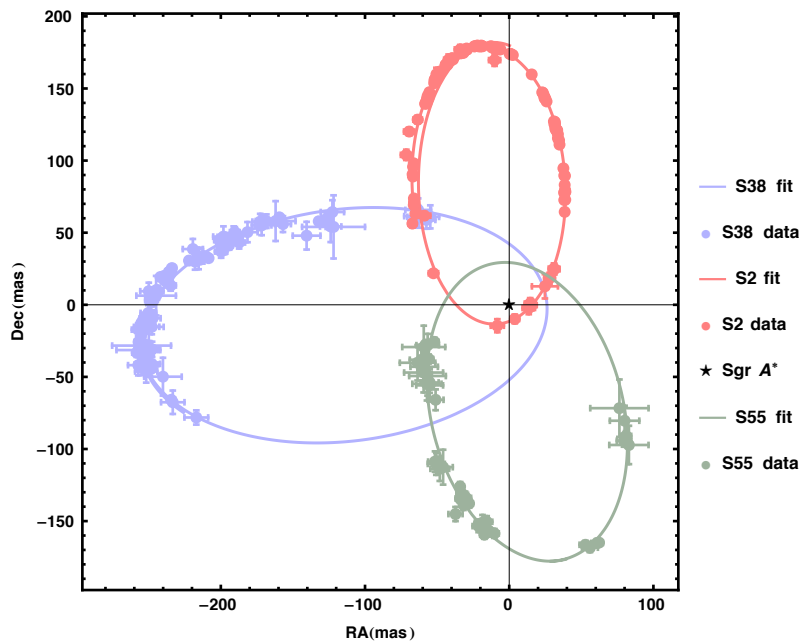


Figure 4: Top panels show the comparison between the observed and fitted coordinates, and bottom panels the corresponding (O-C) residuals for *S2*, *S38* and *S55*.

Schwarzschild value is

$$\Xi = -1.64236 \pm 0.10305 . \quad (\text{IV.1})$$

We next focused on the Galactic center scale to constrain

Figure 5: Best relativistic multi-star orbit fit of  $S2$ ,  $S38$  and  $S55$ .

Star	$\Xi$
$S2$	$-5900^{+39358.8}_{-44964.9}$
$S38$	$25500^{+22607.1}_{-23312.88}$
$S55$	$60400^{+81386}_{-87446.9}$
Multi-Star	$17400^{+30555.6}_{-32244.3}$

Table VII: Best-fit values for  $\Xi$ .

$\Xi$  by investigating the orbital motion of  $S$ -stars. We used a fully relativistic approach based on an agnostic method: for each value of  $\Xi$ , we solved the geodesic equations numerically starting from initial conditions at the apocenter. After applying the Thiele-Innes formulas to the mock positions, we were able to compare the resulting solution with the observed stellar orbits. Finally, we quantified the discrepancy between the simulated and observed orbits performing a  $\chi^2$ -statistics. The inferred confidence region for  $\Xi$  is compatible with the bounds obtained by the precession analysis, and thus with General Relativity. Indeed we found  $17400^{+30555.6}_{-32244.3}$ . Since  $S$ -stars are at a distance of about  $r > 1000 R_g$  from the source, strong field effects are not relevant and such a result was expected.

The proposed approach is completely general and represents a useful tool in the classification of Extended Theories of Gravity. Moreover, this approach has already been used to test a Yukawa-like gravitational potential by means of dynamical tests at the Galactic Centre [38–41], where no significant deviations from General Relativity were found either. Nevertheless, the definitive confirmation (or exclusion) of a given

Extended Theory of Gravity requires the improvement of the constraints on its free parameters based on the observation of various strong field effects. This task can be accomplished taking advantage of the increasing high accuracy observations of second generation instruments like GRAVITY [42].

In particular, we focus on finding stars with short semi-major axis and highly eccentric orbits within the pericenter of  $S2$ . The existence of such a population of stars can be inferred from the recent discovery of the sources  $S62$ ,  $S4711$  and  $S4714$  [43, 44]. Observing stars at smaller radii is essential to detect strong field effects, which become no longer negligible for distances of the pericenter  $r \simeq 10 R_g$ , and therefore any deviations from General Relativity to find out the underlying gravitational theory.

### Acknowledgments

R.C. is partially supported by the INFN Iniziativa Specifica FLAG. M.D.L. and A.D. acknowledges INFN Sezione di Napoli (Iniziativa Specifica TEONGRAV). A.G. is supported by the European Union’s Horizon 2020 research and innovation programme under the Marie Skłodowska-Curie Actions (grant agreement No. 895648–CosmoDEC). The work of R.C. and A.G. has also been carried out in the framework of activities of the National Group of Mathematical Physics (GNFM, INdAM).

[1] S. W. Hawking and G. F. R. Ellis, “The Large Scale Structure of Space-Time,” (Cambridge University Press, Cambridge, 1973)

[2] R. P. Geroch and J. H. Traschen, Phys. Rev. D **36**, 1017 (1987)

- [Conf. Proc. C **861214**, 138 (1986)].
- [3] R. Casadio, M. Lenzi and O. Micu, Phys. Rev. D **98**, 104016 (2018) [arXiv:1806.07639 [gr-qc]].
- [4] R. Casadio and I. Kuntz, Eur. Phys. J. C **80**, 581 (2020) [arXiv:2003.03579 [gr-qc]].
- [5] S. Weinberg, “Gravitation and Cosmology: Principles and Applications of the General Theory of Relativity,” (Wiley & Sons, 1972)
- [6] S. Deser, Gen. Rel. Grav. **1**, 9 (1970) [gr-qc/0411023]; Gen. Rel. Grav. **42**, 641 (2010) [arXiv:0910.2975 [gr-qc]].
- [7] R. P. Feynman, F. B. Morinigo, W. G. Wagner and B. Hatfield, “Feynman lectures on gravitation,” (Addison-Wesley Publishing Company, Reading, 1995)
- [8] R. M. Wald, Phys. Rev. D **33**, 3613 (1986); K. Heiderich and W. Unruh, Phys. Rev. D **38**, 490 (1988); M. P. Hertzberg, JHEP **1709**, 119 (2017) [arXiv:1702.07720 [hep-th]]; D. Bai and Y. H. Xing, Nucl. Phys. B **932**, 15 (2018) [arXiv:1610.00241 [hep-th]]; R. Carballo-Rubio, F. Di Filippo and N. Moynihan, JCAP **1910**, 030 (2019) [arXiv:1811.08192 [hep-th]]; D. Hansen, J. Hartong and N. A. Obers, Phys. Rev. Lett. **122**, 061106 (2019) [arXiv:1807.04765 [hep-th]].
- [9] R. Casadio, M. Lenzi and O. Micu, Eur. Phys. J. C **79**, 894 (2019) [arXiv:1904.06752 [gr-qc]].
- [10] R. Casadio and O. Micu, Phys. Rev. D **102**, 104058 (2020) [arXiv:2005.09378 [gr-qc]].
- [11] R. Casadio, O. Micu and J. Mureika, Mod. Phys. Lett. A **35**, 2050172 (2020) [arXiv:1910.03243 [gr-qc]].
- [12] R. Casadio, A. Giugno and A. Giusti, Phys. Lett. B **763**, 337 (2016) [arXiv:1606.04744 [gr-qc]].
- [13] R. Casadio, A. Giugno, A. Giusti and M. Lenzi, Phys. Rev. D **96**, 044010 (2017) [arXiv:1702.05918 [gr-qc]].
- [14] R. Casadio, M. Lenzi and A. Ciarfella, Phys. Rev. D **101**, 124032 (2020) [arXiv:2002.00221 [gr-qc]].
- [15] G. Dvali and C. Gomez, Fortsch. Phys. **61**, 742 (2013) [arXiv:1112.3359 [hep-th]]; G. Dvali, C. Gomez and S. Mukhanov, “Black Hole Masses are Quantized,” arXiv:1106.5894 [hep-ph]. G. Dvali and C. Gomez, Phys. Lett. B **719**, 419 (2013) [arXiv:1203.6575 [hep-th]]; Phys. Lett. B **716**, 240 (2012) [arXiv:1203.3372 [hep-th]]; Eur. Phys. J. C **74**, 2752 (2014) [arXiv:1207.4059 [hep-th]]; A. Giusti, Int. J. Geom. Meth. Mod. Phys. **16**, 1930001 (2019).
- [16] R. Casadio, A. Giusti, I. Kuntz and G. Neri, Phys. Rev. D **103**, 064001 (2021) [arXiv:2101.12471 [gr-qc]].
- [17] M. Cadoni, R. Casadio, A. Giusti, W. Mück and M. Tuveri, Phys. Lett. B **776**, 242 (2018) [arXiv:1707.09945 [gr-qc]].
- [18] I. De Martino, R. Lazkoz and M. De Laurentis, Phys. Rev. D **97**, 104067 (2018) [arXiv:1801.08135 [gr-qc]].
- [19]
- [20] C. M. Will, Phys. Rev. Lett. **120**, 191101 (2018) [arXiv:1802.05304 [gr-qc]].
- [21] T. D. Moyer, “Mathematical formulation of the Double-Precision Orbit Determination Program (DPODP),” Technical Report 32-1527 (NASA Jet Propulsion Laboratory, Pasadena, 1971).
- [22] T. D. Moyer, “Formulation for observed and computed values of Deep Space Network data types for navigation,” JPL Publication 00-7 (NASA Jet Propulsion Laboratory, Pasadena, 2000).
- [23] A. Eckart and R. Genzel, Nature **383**, 415 (1996).
- [24] A. M. Ghez, S. Salim, N. N. Weinberg, J. R. Lu, T. Do, J. K. Dunn, K. Matthews, M. Morris, S. Yelda and E. E. Becklin, *et al.* Astrophys. J. **689**, 1044 (2008) [arXiv:0808.2870 [astro-ph]].
- [25] A. Eckart and R. Genzel, Mon. Not. Roy. Astron. Soc. **284**, 576 (1997).
- [26] S. Gillessen, F. Eisenhauer, S. Trippe, T. Alexander, R. Genzel, F. Martins and T. Ott, Astrophys. J. **692**, 1075 (2009) [arXiv:0810.4674 [astro-ph]].
- [27] S. Gillessen, F. Eisenhauer, T. K. Fritz, H. Bartko, K. Dodds-Eden, O. Pfuhl, T. Ott and R. Genzel, Astrophys. J. Lett. **707**, L114 (2009) [arXiv:0910.3069 [astro-ph.GA]].
- [28] A. M. Ghez, B. L. Klein, M. Morris and E. E. Becklin, Astrophys. J. **509**, 678 (1998) [arXiv:astro-ph/9807210 [astro-ph]].
- [29] R.L. Arnowitt, S. Deser and C.W. Misner, Phys. Rev. **116**, 1322 (1959).
- [30] S. Gillessen, P.M. Plewa, F. Eisenhauer, R. Sari, I. Waisberg, M. Habibi, O. Pfuhl, E. George, J. Dexter, S. von Fellenberg, *et al.* Astrophys. J. **837**, 30 (2017) [arXiv:1611.09144 [astro-ph.GA]].
- [31] R. Schodel, T. Ott, R. Genzel, A. Eckart, N. Mouawad and T. Alexander, Astrophys. J. **596**, 1015 (2003) [arXiv:astro-ph/0306214 [astro-ph]].
- [32] S. Gillessen, F. Eisenhauer, T. K. Fritz, H. Bartko, K. Dodds-Eden, O. Pfuhl, T. Ott and R. Genzel, Astrophys. J. Lett. **707**, L114 (2009) [arXiv:0910.3069 [astro-ph.GA]].
- [33] R. Abuter *et al.* [GRAVITY], Astron. Astrophys. **636**, L5 (2020) [arXiv:2004.07187 [astro-ph.GA]].
- [34] W.M. Smart Mon. Not. Roy. Astron. Soc. **90**, 534 (1930).
- [35] W.M. Smart “The Binary Stars,” (1964)
- [36] G.G. Nyambuya, Mon. Not. Roy. Astron. Soc. **451**, 3034 (2015).
- [37] E.V. Pitjeva, N.P. Pitjev Mon. Not. Roy. Astron. Soc. **432**, 3431 (2013).
- [38] I. de Martino, R. della Monica and M. de Laurentis, “ $f(R)$ -gravity after the detection of the orbital precession of the S2 star around the Galactic centre massive black hole,” arXiv:2106.06821 [gr-qc].
- [39] A. D’Addio, Phys. Dark Univ. **33**, 100871 (2021).
- [40] I. De Martino, R. Lazkoz and M. De Laurentis, Phys. Rev. D **97**, 104067 (2018) [arXiv:1801.08135 [gr-qc]].
- [41] R. Della Monica, I. de Martino and M. de Laurentis, “Orbital precession of the S2 star in Scalar-Tensor-Vector-Gravity,” arXiv:2105.12687 [gr-qc].
- [42] S. Gillessen, F. Eisenhauer, G. Perrin, W. Brandner, C. Straubmeier, K. Perraut, A. Amorim, M. Schöller, C. Araujo-Hauck and H. Bartko, *et al.* Proc. SPIE Int. Soc. Opt. Eng. **7734**, 77340Y (2010) [arXiv:1007.1612 [astro-ph.IM]].
- [43] F. Peissker, A. Eckart and M. Parsa Astrophys. J. **889**, 61 (2020) [arXiv:2002.02341 [astro-ph.GA]].
- [44] F. Peissker, A. Eckart, M. Zajacek, B. Ali and M. Parsa Astrophys. J. **899**, 50 (2020).